

Cosmic evolution of bars in simulations of galaxy formation

Takashi OKAMOTO¹

¹*Department of Cosmosciences, Graduate School of Science, Hokkaido University, N10 W8, Kitaku, Sapporo, 060-0810, Japan
okamoto@astro1.sci.hokudai.ac.jp*

Mari ISOE^{2,3}

²*Department of Astronomy, School of Science, The University of Tokyo, 7-3-1 Hongo, Bunkyo-ku, Tokyo 113-0033*

³*Division of Theoretical Astronomy, National Astronomical Observatory of Japan, 2-21-1 Osawa, Mitaka, Tokyo 181-8588
isoe.mari@nao.ac.jp*

and

Asao HABE¹

habe@astro1.sci.hokudai.ac.jp

(Received ; accepted)

Abstract

We investigate the evolution of two bars formed in fully self-consistent hydrodynamic simulations of the formation of Milky Way-mass galaxies. One galaxy shows higher central mass concentration and has a longer and stronger bar than the other at $z = 0$. The stronger bar evolves by transferring its angular momentum mainly to the dark halo. Consequently the rotation speed of the bar decreases with time, while the amplitude of the bar increases with time. These features qualitatively agree with the results obtained by idealized simulations. The pattern speed of the stronger bar largely goes up and down within a half revolution in its early evolutionary stage. These oscillations occur when the bar is misaligned with the $m = 4$ mode Fourier component. These oscillations correlate with the oscillations in the triaxiality of the dark matter halo, but differently from the way identified by idealized simulations. The amplitude of the weaker bar does not increase despite the fact that its rotation slows down with time. This result contradicts what is expected from idealized simulations and is caused by the decline of the central density associated with the mass loss and feedback from the stellar populations. The amplitude of the weaker bar is further weakens by the angular momentum injection by the interactions with stellar clumps in the disk. In the both galaxies, the bars are terminated around the 4:1 resonance.

Key words: cosmology: theory – galaxies: formation – galaxies: evolution – galaxies: structure–methods: numerical

1. Introduction

Roughly two-thirds of disk galaxies have bars, of which half have strong bars today (Eskridge et al. 2000; Barazza et al. 2008). The bar fraction seems to be a strong function of redshift; it decreases by a factor of three from $z = 0$ to $z = 0.8$ (Sheth et al. 2008). Bars can affect galaxy properties by driving secular evolution (e.g. Kormendy 1979; Combes & Sanders 1981; Pfenniger & Norman 1990; Combes & Elmegreen 1993; Debattista et al. 2004; Kormendy & Kennicutt 2004; Athanassoula 2005; Athanassoula 2013; Kormendy 2013), and thus a number of simulations have performed to study their formation and evolution processes.

Most of the simulations employ idealized initial conditions for isolated galaxies in order to answer specific questions (e.g. Combes et al. 1990; Debattista & Sellwood 2000; Athanassoula 2003; Martinez-Valpuesta et al. 2006; Athanassoula et al. 2013). A general picture obtained by these studies is that a bar continuously grows and slows down with time as its angular momentum gets transferred to the dark halo and the outer disk (e.g. Weinberg 1985; Combes & Elmegreen 1993; Athanassoula

2003).

In reality however disks and dark halos keep growing while bars form and evolve. The dark halos resulting from cosmological simulations are naturally triaxial (Frenk et al. 1988; Jing & Suto 2002) and abundant in substructure (Moore et al. 1999; Klypin et al. 1999; Springel et al. 2008), both of which should exert torque on bars. Galaxy interactions could trigger bar formation (Miwa & Noguchi 1998; Berentzen et al. 2004). Moreover, even disk orientation changes with time owing to the misalignment of the angular momentum vector of the newly accreting gas (Okamoto et al. 2005; Okamoto 2013).

Early attempts to investigate the effects of cosmological growth of galaxies on the bar evolution are made either by simplifying the initial density perturbations (Heller et al. 2007a; Romano-Díaz et al. 2008) or by embedding a live disk in a growing dark halo (Curir et al. 2006). Kraljic et al. (2012) use a cosmological N -body simulation as boundary conditions for sticky particle simulations and follow galaxy and bar evolution in evolving halos. They confirm that the bar fraction in fact decreases with increasing redshift. Scannapieco & Athanassoula (2012) analyze the bars in fully self-consistent simulations of galaxy

formation at $z=0$ and compare their properties with those in the idealized simulations.

Only recently have cosmological simulations with sufficient resolution to follow evolution of detailed structure in disk galaxies become possible (Guedes et al. 2011; Okamoto 2013; Stinson et al. 2013; Marinacci et al. 2014). An important difference of these simulations from the idealized simulations is that they invoke much stronger stellar feedback than the idealized simulations normally assume, otherwise simulations form too many stars for a given halo mass (e.g. Scannapieco et al. 2012; Okamoto 2013; Okamoto et al. 2014). The feedback is so strong that it can lower the central stellar and dark matter density during the galaxy evolution (Duffy et al. 2010; Governato et al. 2012), and hence orbits of stars should be affected.

Two Milky Way-mass galaxies formed in the cosmological simulations by Okamoto (2013) offer a unique opportunity to investigate the evolution of bars in the context of the Λ -cold dark matter (Λ CDM) cosmology. One galaxy is clearly barred from $z \simeq 1$ to 0, while the other has a much weaker bar. In this paper we compare and contrast these two galaxies focusing on the evolution of their bars. We also compare their properties with those obtained by idealized simulations.

This paper is organized as follows. In section 2 we briefly describe the simulations and galaxies we analyze. We present our results in section 3. We then discuss them and summarize our main conclusion in section 4.

2. Sample galaxies

We study the evolution of the bars formed in two smoothed particle hydrodynamic (SPH) simulations of galaxy formation in a Λ CDM universe. The cosmological parameters employed in these simulations are: $\Omega_0 = 0.25$, $\Omega_\Lambda = 0.75$, $\Omega_b = 0.045$, $\sigma_8 = 0.9$, $n_s = 0.9$, and a Hubble constant of $H_0 = 100 h \text{ km s}^{-1} \text{ Mpc}^{-1}$, where $h = 0.73$. The galaxies are selected from a cosmological periodic box of a side length of $100 h^{-1} \text{ Mpc}$ and called ‘Aq-C’ and ‘Aq-D’ according to the labeling system of the Aquarius project (Springel et al. 2008).

The dark matter particle masses are 2.6×10^5 and $2.2 \times 10^5 M_\odot$ for Aq-C and Aq-D, respectively, and the original SPH particle masses are 5.8×10^4 and $4.8 \times 10^4 M_\odot$, respectively. At $z < 3$ the gravitational softening lengths are fixed in physical coordinates as $\epsilon = 0.257$ and 0.240 kpc respectively in Aq-C and Aq-D. The simulations include radiative cooling, photo-heating by the ultra-violet background (Okamoto et al. 2008), star formation, timed release of energy, mass, and metals by type II and Ia supernovae and AGB stars (Okamoto et al. 2010; Okamoto 2013). It should be noted that the mass resolution of our simulations are as good as that in the high resolution idealized simulations, but the spatial resolution is still poor compared with that of the recent idealized simulations (50 pc in Athanassoula et al. 2013).

The way of implementing feedback is a key to reproduce observed properties of galaxies (Okamoto et al. 2010; Okamoto et al. 2014). In our simulations, the en-

ergetic feedback from supernovae is modelled as winds. A gas particle may receive an amount of energy, ΔE , from type II supernovae during a time-step, Δt . We add this gas particle to winds with a probability, $p_w = \Delta E / [(1/2)m_{\text{gas}}v_w^2]$, where m_{gas} is the mass of the gas particle and v_w is the initial wind speed. The initial wind speed, v_w is given as $v_w = 5\sigma$, where σ is the one-dimensional velocity dispersion of the dark matter particles around the gas particle.

Doing this ensures that the wind mass generated by a type II supernova is proportional to σ^{-2} , and therefore less mass galaxies blow more winds per unit star formation than their more massive counterparts. This feedback model explains luminosities and metallicities of galaxies ranging from the Local Group satellites (Okamoto et al. 2010) to more massive galaxies (Okamoto et al. 2014). The supernova feedback implemented this way is the strongest among the simulations presented in Scannapieco et al. (2012), and the resulting stellar mass of the galaxies is consistent with what expected by the abundance matching for their halo masses. (Guo et al. 2010; Behroozi et al. 2013; Moster et al. 2013).

The simulations follow the evolution of the stellar populations throughout their entire life. Therefore the star particles lose their masses not only by the type II supernovae and mass loss from the massive stars but also by type Ia supernovae and the stellar mass loss from the intermediate mass stars. The feedback from old stellar populations by type Ia supernovae is also considered.

The stellar masses of these galaxies at $z = 0$ are $4.0 \times 10^{10} M_\odot$ (Aq-C) and $3.1 \times 10^{10} M_\odot$ (Aq-D); hence their masses are close to that of the Milky Way. The global evolution and properties of these galaxies are fully described in Okamoto (2013). We here only show the evolution of the circular velocity profiles which is the most relevant to the current study.

In order to characterize the mass distribution and the angular frequency of circular orbits, we calculate the circular velocity from the azimuthally averaged radial acceleration in the disk plane, $a_r(r)$, as $v_c(r)^2 = -ra_r(r)$. We measure the radial acceleration at equally spaced 128 azimuthal positions at each radius in the disk plane to determine $a_r(r)$.

We show the evolution of the circular velocity measured this way in figure 1. We find that the central circular velocity continuously decreases with time in both galaxies. This is presumably due to the stellar mass loss and feedback since we do not find this behavior in simulations without stellar mass loss nor feedback. This drop changes the resonance structure as we will show later. We also find that Aq-C has more centrally concentrated mass distribution than Aq-D.

The vertical line indicates the radius inside which a baryonic component dominates as $v_c(r) < 1.1v_{c,b}(r)$, where $v_{c,b}(< r)$ is the contribution of the baryons (gas and stars) to the circular velocity; the disks are bar unstable when this condition is satisfied (Efsthathiou et al. 1982), although this criterion is only appropriate for a pure N -body cold disk in a rigid halo (e.g. Athanassoula 2008).

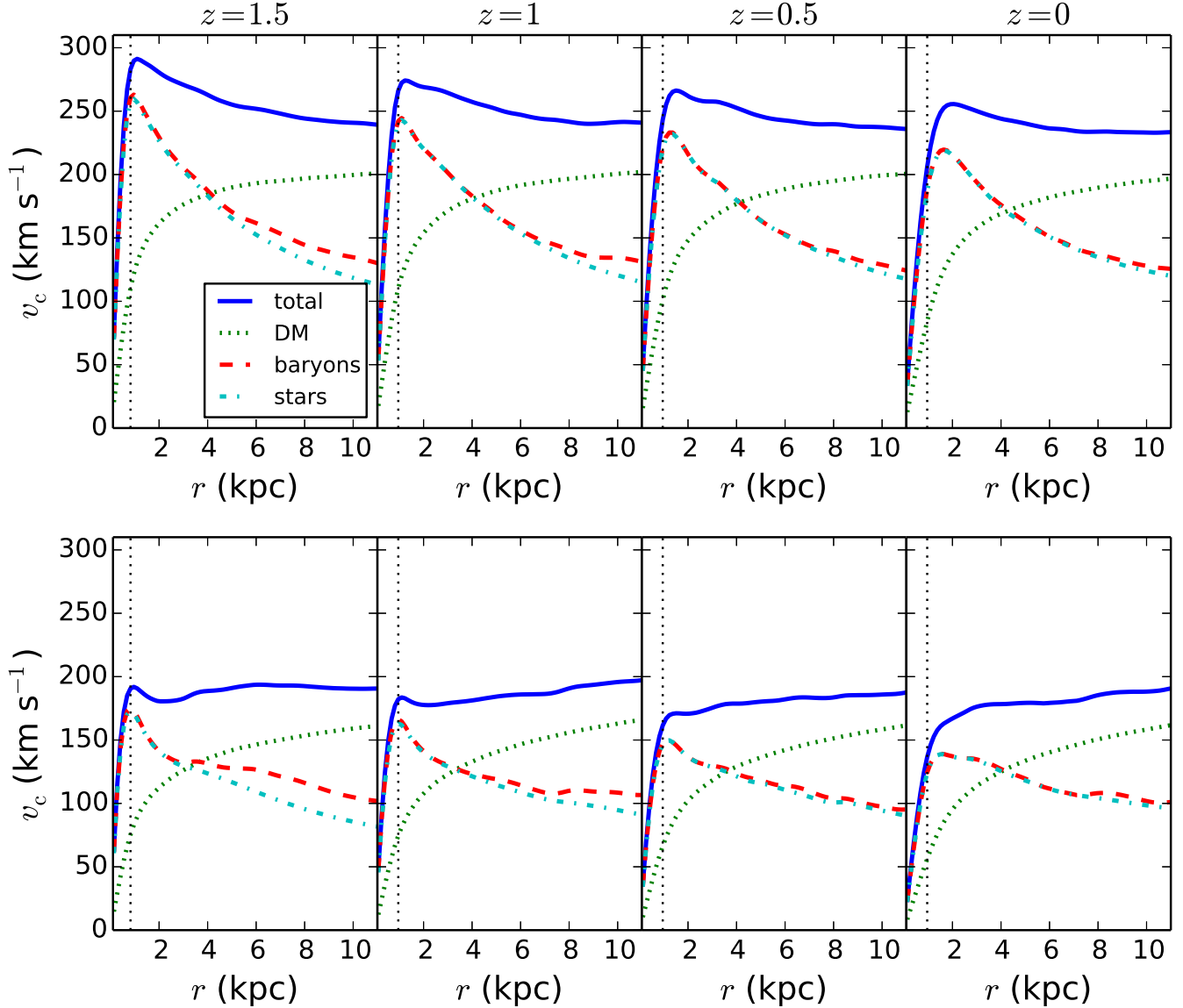


Fig. 1. Evolution of the circular velocity profiles. The upper and lower panels show Aq-C and Aq-D, respectively. From left to right, the circular velocities at $z = 1.5$, 1.0 , 0.5 , and 0 are plotted as functions of radius. The blue solid lines are the circular velocities calculated from the azimuthally averaged radial accelerations in the disk planes, and the green dotted, red dashed, and cyan dot-dashed lines indicate the contribution of the dark matter, baryons, and stellar components, respectively. The vertical dotted lines indicate the radii at which $v_c(r) = 1.1v_{c,b}(r)$, where $v_{c,b}(r)$ is the contribution of the baryonic matter to the circular velocity at the radius, r .

This radius is almost constant with redshift ($\simeq 1$ kpc) in both galaxies. Similarly, the radius at which the contribution of the baryons is equal to that of the dark matter is also constant with redshift ($\simeq 4$ kpc), indicating that the stellar mass fractions as functions of radius do not evolve strongly with redshift. Aq-C's circular velocity curve is more resembling to the universal rotation curve proposed by Salucci et al. (2007) than Aq-D's.

3. Results

In this section, we first describe how we identify stellar bars in the simulated galaxies and then undertake detailed studies of the evolution of the bars. In the following analyses, the z -direction is chosen to be parallel to the angular momentum vector of stars within 5 per cent of the virial radius¹ at given redshift unless otherwise stated. Note that the disk orientation significantly changes with redshift (Okamoto et al. 2005; Okamoto 2013). We use stars with $|z| < 1 h^{-1}$ kpc to compute the surface stellar density to avoid the contamination of the stars in the satellite galaxies.

3.1. Bar identification

The strength, length, and angle of a bar can be parameterized by the amplitude and phase of its Fourier component, defined by expressing the surface stellar density as a Fourier series,

$$\frac{\Sigma(r, \phi)}{\bar{\Sigma}(r)} = 1 + \sum_{m=1}^{\infty} A_m(r) \cos[m\{\phi - \phi_m(r)\}], \quad (1)$$

where $\Sigma(r, \phi)$ is the surface stellar density, ϕ is the azimuthal angle, $\bar{\Sigma}(r)$ is the azimuthally averaged surface stellar density at radius r , and A_m and ϕ_m are the amplitude and phase of the m -th Fourier component, respectively. Before we perform this analysis, we remove stellar clumps in order for the $m = 2$ component not to include contributions of them, which are particularly abundant in Aq-D (Okamoto 2013). The details of this procedure and its effect are described in appendix 1. In short, the removal of the clumps does not affect our results presented in this paper. We calculate the Fourier series for the face-on projections.

Typically, the amplitude of the $m = 2$ mode, $A_2(r)$, has a peak if a bar exists. The phase, $\phi_2(r)$, should be constant in the bar region. We first identify the radius at which $A_2(r)$ takes the maximum value, A_2^{\max} , and we call this radius r_2^{\max} . The bar angle is defined as $\phi_{\text{bar}} = \phi_2(r_2^{\max})$. We utilize the radial profile of the phase of the $m = 2$ Fourier component to determine the bar length. Outside the bar region, the phase should show large variation owing to a spiral structure or by the absence of clear structure. We thus define the bar length, r_{bar} , as the maximum radius where the bar angle ϕ_{bar} and the phase of the $m = 2$ component differ by less than $\Delta\phi$. We employ $\Delta\phi = 0.1\pi$ in this paper.

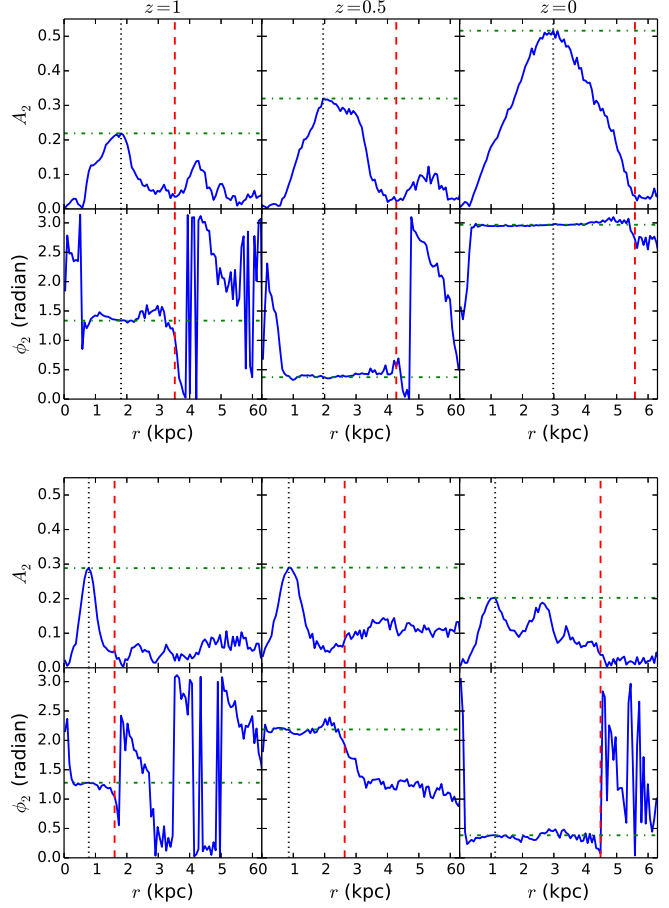


Fig. 2. The amplitude and phase profiles of the $m = 2$ mode. The upper and lower six panels show Aq-C and Aq-D, respectively. From left to right, the results at $z = 1, 0.5,$ and 0 are presented. The bar length, r_{bar} , is indicated by the vertical red dashed line in each panel. The horizontal green dot-dashed lines indicate the values of A_2^{\max} and ϕ_{bar} in the panels for amplitude and phase, respectively.

Athanassoula & Misiriotis (2002) present a number of ways to measure bar length; each method has its own pros and cons. Scannapieco & Athanassoula (2012) compare three methods among them, which are readily applicable to disks obtained by cosmological simulations. We also compare these three methods in appendix 2; the first method is what we have described above, the second method uses the $m = 2$ amplitude profiles, and the third method compares the surface stellar density profile along the bar major axis with that along the bar minor axis. We find that the bar lengths obtained by these three methods agree reasonably well.

We demonstrate our method in figure 2 where we plot the amplitude and phase profiles of the $m = 2$ Fourier component at $z = 1, 0.5,$ and 0 . We find that the amplitude, $A_2(r)$, has a clear peak at each redshift and the phase, $\phi_2(r)$, is nicely constant around the peak. We hence conclude that both A_2^{\max} and ϕ_{bar} are robustly defined by this method.

On the other hand, the bar length, r_{bar} , has weak

¹ The virial radius is calculated based on the spherical collapse model (Eke et al. 1996).

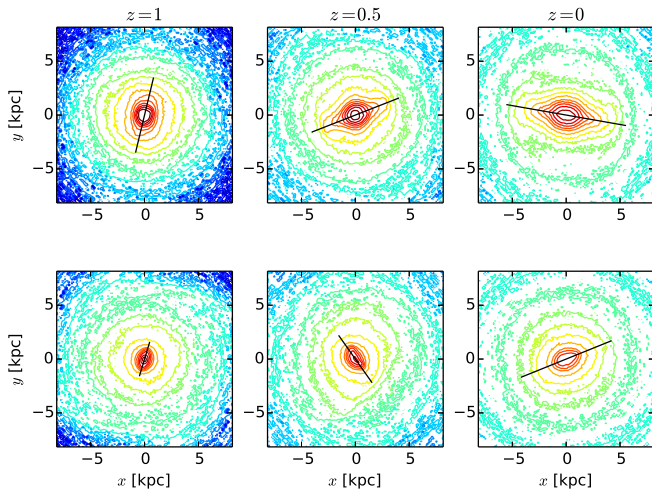


Fig. 3. Contour maps of the face-on stellar surface density of the galaxies. We have removed the clumps from the density distributions as described in appendix 1. The upper and lower panels correspond to Aq-C and Aq-D, respectively, and the galaxies at $z = 1, 0.5,$ and 0 are shown from left to right. The contour levels are logarithmic. The black solid lines indicate the bars whose length and angle are defined as described in the text.

dependence on the value of $\Delta\phi$, and thus it is less robustly defined². In Aq-D, the amplitude, $A_2(r)$, has two peaks within the bar length at $z = 0$. Such a feature is hardly seen either in real galaxies (e.g. Buta et al. 2006; Elmegreen et al. 2007; Buta et al. 2009) or in the idealized simulations (e.g. Athanassoula & Misiriotis 2002). We therefore examine whether the outer peak is a different component from the inner component, which is coincidentally aligned with the inner component in appendix 3.

We find that the amplitude of the outer peak shows a rapid time variation and the outer component always has almost the same phase as the inner component. By inspecting the surface density distribution, we speculate that the outer $m = 2$ peak is induced by interactions with the debris of the stellar clumps in the outer region of the bar, which is orbiting with the different angular velocity from the bar. We thus hold our definition of the bar length throughout this paper. We will later show how the bar length changes if we exclude the outer component. It should be noted that we always use the inner component to define the bar angle and amplitude of Aq-D, and therefore the treatment of the outer component does not affect most of the results and discussions presented in this paper.

The bars identified this way are overplotted on the face-on surface stellar density maps in figure 3. The surface stellar density maps confirm that Aq-C always has a longer bar than Aq-D, while Aq-D has a better defined bar at $z = 1$, which is evident from figure 2 where the value of A_2^{\max} of Aq-D at $z = 1$ is larger than that of Aq-C. We find that the central surface stellar density decreases with

² Any methods described in appendix 2 introduce a tolerance parameter to define the bar length.

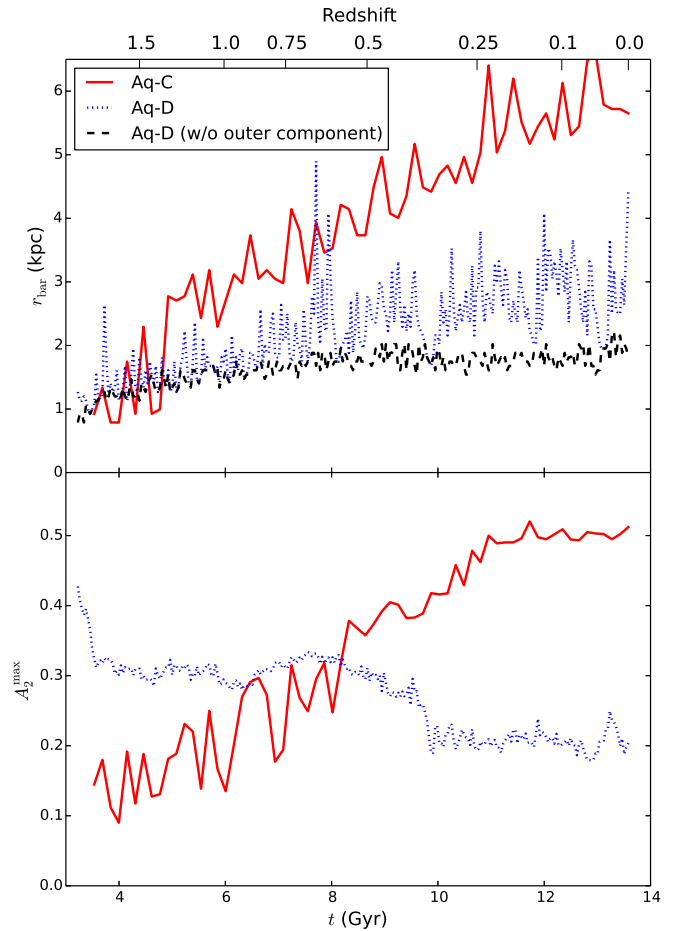


Fig. 4. Time evolution of the bar length, r_{bar} , and the amplitude, A_2^{\max} . The upper panel shows the bar lengths as functions of time (or redshift). The red solid and blue dotted lines indicate Aq-C and Aq-D, respectively. The black dashed line represents the bar length of Aq-D when we exclude the outer component. The amplitude, A_2^{\max} , is shown in the lower panel.

time in both galaxies. We also find that Aq-D has more structure than Aq-C such as spiral arms. Such structure in Aq-D is mainly induced by the interactions with the clumps (see appendix 1), which we have erased in figure 3.

The clumps sink to the central region (Okamoto 2013), and it can change the bar properties by adding mass and changing the angular momentum of the central region. By comparing the bar lengths and angles indicated by the straight lines in figure 3 with the shapes of the isodensity contours, we conclude that our method identifies the bars in the simulated galaxies well.

3.2. Redshift evolution

We now investigate the redshift evolution of the bars. We plot the bar lengths, r_{bar} , and the bar amplitudes, A_2^{\max} , as functions of cosmic time and redshift in figure 4. We find that Aq-C's bar becomes longer and stronger with time. This behavior is usually seen for bars in early-type disk galaxies (Combes & Elmegreen 1993) or bars in galaxies with centrally concentrated dark halos in the ideal-

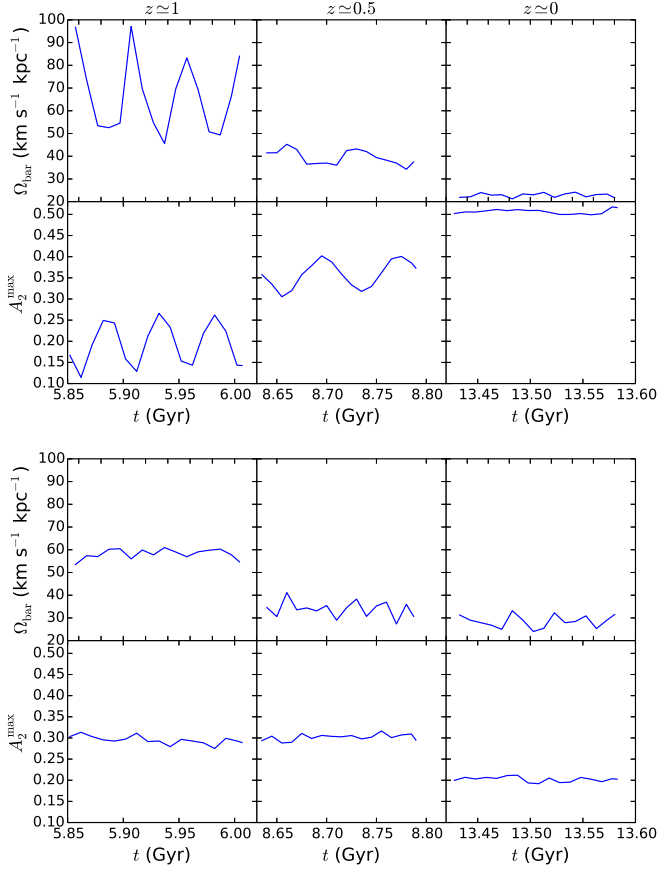


Fig. 5. Time evolution of the bar pattern speed, Ω_{bar} , and the amplitude, A_2^{max} , around $z = 1$, 0.5, and 0 (from left to right). We show Aq-C and Aq-D in the upper and lower six panels, respectively. The bar pattern speed and the amplitude are respectively shown in the upper and lower three panels of each group of panels as functions of cosmic time.

ized simulations (Athanasoula 2003). This is consistent with the fact that Aq-C has a massive bulge (Okamoto 2013) and its halo shows the high central concentration (figure 1).

Contrarily, Aq-D’s bar does not show such strong evolution in the length and its amplitude is almost constant until $t \sim 9.8$ Gyr, around which it sharply drops to the lower value. We also compute the bar length in Aq-D by excluding the component corresponding to the outer peak. To do so, we find the radius between the inner and outer peaks at which the amplitude, $A_2(r)$, takes the minimum value. If this radius is shorter than the bar length defined by the phase profile, we employ this radius as the bar length. The bar length defined this way exhibits very weak time evolution. The comparison between two bar lengths with the different definitions implies that the outer region of Aq-D’s bar is violently disturbed by the interactions with the stellar clumps. We will show both bar lengths when the bar length is matter.

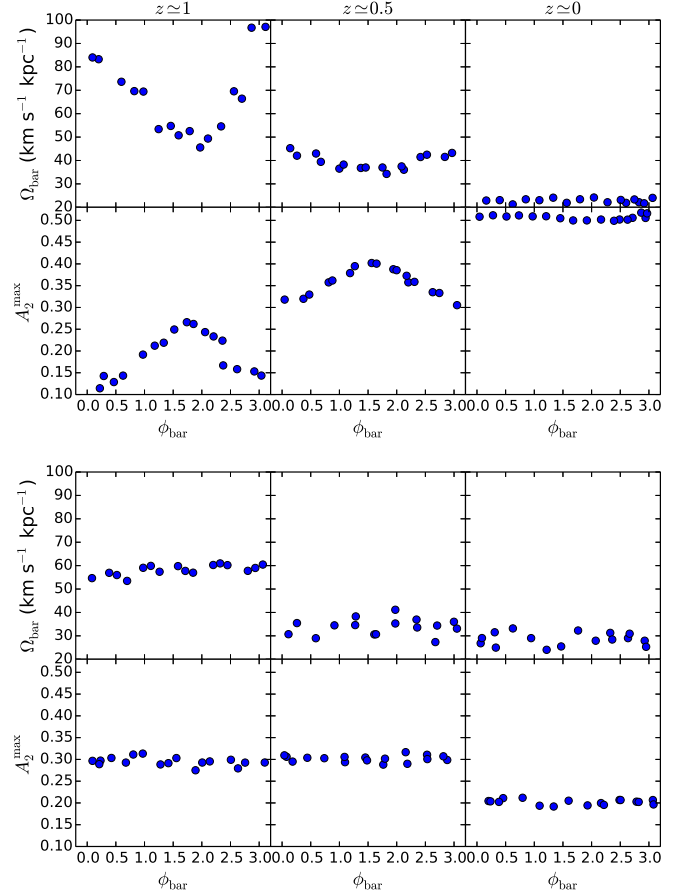


Fig. 6. Same as figure 5 but now as functions of the bar angle, ϕ_{bar} .

3.3. Pattern speed of the bars

The time-steps used to output the simulation snapshots are too large to measure the bar pattern speed. Moreover, the change of the disk orientation with time (Okamoto 2013) makes it difficult to measure the pattern speed. We hence restart the simulations around $z = 1$, 0.5, and 0, and then follow their evolution for a short period of time during which the orientation of the disks hardly changes; when the rotation axis of the disk is most misaligned with the initial one, the cosine of the angle between them is 0.996, which occurs in the simulation for Aq-C at $z \sim 1$. In other simulations this value is always greater than 0.999. The disk does not tumble during these periods, and thus the misalignment monotonically increases with time. We employ the output time-step of 10 Myr for these additional simulations.

In figure 5 we show the bar pattern speed, $\Omega_{\text{bar}} \equiv \dot{\phi}_{\text{bar}}$, and the amplitude, A_2^{max} , as functions of time around $z = 1$, 0.5 and 0. Firstly, we find that the pattern speed of the bars slows down from $z = 1$ to 0 in both galaxies. The long-term behavior of Aq-C’s bar is consistent with what we expect from the results of the idealized simulations, that is, the bar becomes stronger and longer as it rotates more slowly. Aq-D’s bar however does not change its amplitude

between $z \simeq 1$ and 0.5 while its pattern speed decreases. the bar amplitude becomes smaller from $z \simeq 0.5$ to 0.

The pattern speed and the amplitude of Aq-C's bar display large oscillations at $z \simeq 1$ and 0.5. Interestingly, the short-term behavior is similar to the long-term one, i.e. the bar gets stronger when the pattern speed decreases. This oscillation becomes smaller with time and almost vanishes at $z \simeq 0$. Such oscillations have also been observed in idealized simulations (Dubinski et al. 2009; Athanassoula et al. 2013). Athanassoula et al. (2013) suggest that the oscillation is caused by the interaction between a bar and a host triaxial halo. We will investigate halo properties in section 3.5.

The small oscillations seen in the pattern speed of Aq-D's bar do not correlate with the oscillations of the bar amplitude; the amplitude is more or less constant during each period of time. The time evolution of the direction of the rotation axis is not the reason for the oscillations because the angle with the initial rotation axis (z -direction) is sufficiently small. Moreover this angle monotonically increases with time and does not oscillate. We suspect that the oscillation of the pattern speed of Aq-D's bar is caused by the interactions between the bar and the clumps.

To see the short-term behaviors more closely, we now plot the pattern speed and the amplitude as functions of the bar angle, $\phi_{\text{bar}}(t)$, in figure 6. We find that the periods of the oscillations in the amplitude and the pattern speed are half a revolution period of the bar when they show large oscillations (at $z \simeq 1$ and 0.5 in Aq-C). On the other hand, we do not see such a periodicity for Aq-D's bar.

3.4. Which component obtains the angular momentum?

Since the bar pattern speed slows down from $z = 1$ to 0, we expect that the angular momentum of the bars is transferred to other components, such as outer disks or dark halos. In order to identify which component plays the most important role in spinning down the bars, we try to measure the torque from each component acting on the bars. Doing this is however not straightforward because defining particles that constitute the bar is not a simple task. It is also difficult to relate the measured torque to the change in the bar pattern speed even if we somehow define the particles that belong to the bar, since the angular momentum of the bar, $L_{\text{bar}} = I_{\text{bar}}\Omega_{\text{bar}}$, where I_{bar} is the moment of the inertia of the bar, is different from the total angular momentum of the particles that constitute the bar.

We therefore take a simpler approach. We define the bar region as a disk with the radius, r_{bar} , and the height $1 h^{-1}$ kpc, and then compute the torques acting on the star particles within this region. Since the z -component of the torque acting on an axisymmetric component is zero, the torque mainly operates on the bar as long as the bar is the most significant non-axisymmetric structure in the region. We have checked that we obtain qualitatively equivalent results when we calculate torques on the particles along the bar. We have also confirmed the results does not change qualitatively if we employ the bar length by excluding the outer $m = 2$ component for Aq-D.

In figure 7, we show the z -component of the specific torque from the particles within the virial radius acting on the stars in the bar region as a function of the bar angle, $\phi_{\text{bar}}(t)$. We find that the torque from the dark halo dominates the total torque in Aq-C and it is negative on average; the torque from the dark matter spins down the stars in the bar region more strongly at higher redshift. In Aq-C, the torque from the dark matter shows the periodic change with the period of half a bar revolution period. This behavior suggests that the torque is exerted by the anisotropic distribution of the dark matter.

Although the period with which the torque changes is the same as the period with which the pattern speed changes in Aq-C at $z \simeq 1$ and 0.5, the change in the angular momentum of the stars within the bar region is not directly reflected to the bar pattern speed. In the panels of $z \simeq 1$ and 0.5 for Aq-C, we indicate the bar angle where the bar pattern speed becomes the smallest. We find that, against the intuition, the torque takes the largest negative value where the bar pattern speed becomes the smallest. The pattern speed should be the smallest where the torque changes its sign from minus to plus if the angular momentum of the stars within the bar region were directly reflected to the bar pattern speed. Moreover, the pattern speed of Aq-C's bar at $z \simeq 0$ is almost constant while the torque show the same level of variation as at $z \simeq 1$ and 0. This is a direct consequence of the fact that the bar angular momentum, $I_{\text{bar}}\Omega_{\text{bar}}$, is different physical quantity from the total angular momentum of the particles belonging to the bar as we mentioned earlier.

In Aq-D, the amplitude of the specific torque is much smaller than that in Aq-C. The long-term evolution of the bar pattern speed in Aq-D is thus much more moderate than Aq-C. The torque is not always dominated by the contribution of the dark matter, for example the torque is dominated by the contribution of the stars at $z \simeq 0.5$. This is consistent with the fact that the central density of the dark halo of Aq-D is much lower than that of Aq-C and thus there is less dark matter to absorb the angular momentum of the bar.

Athanassoula (2003) show that the angular momentum is emitted from near-resonant material at the inner Lindblad resonance (ILR), i.e. a bar, and absorbed by mainly by near-resonant material at the corotation and the outer Lindblad resonance in the halo; the near-resonant material in the outer disk also absorbs the angular momentum, but the role the outer disk plays is much less significant than the halo. This picture is in good agreement with the analytic calculations (Lynden-Bell & Kalnajs 1972; Tremaine & Weinberg 1984). Our results show that the halo is the main absorber of the angular momentum when a significant amount of the angular momentum of the bar is transferred from the bar. The results thus qualitatively agree with those by the idealized simulations and the prediction of the analytic calculations.

3.5. Halo properties

Athanassoula et al. (2013) claim that the oscillations seen in the bar amplitude can be understood by the inter-

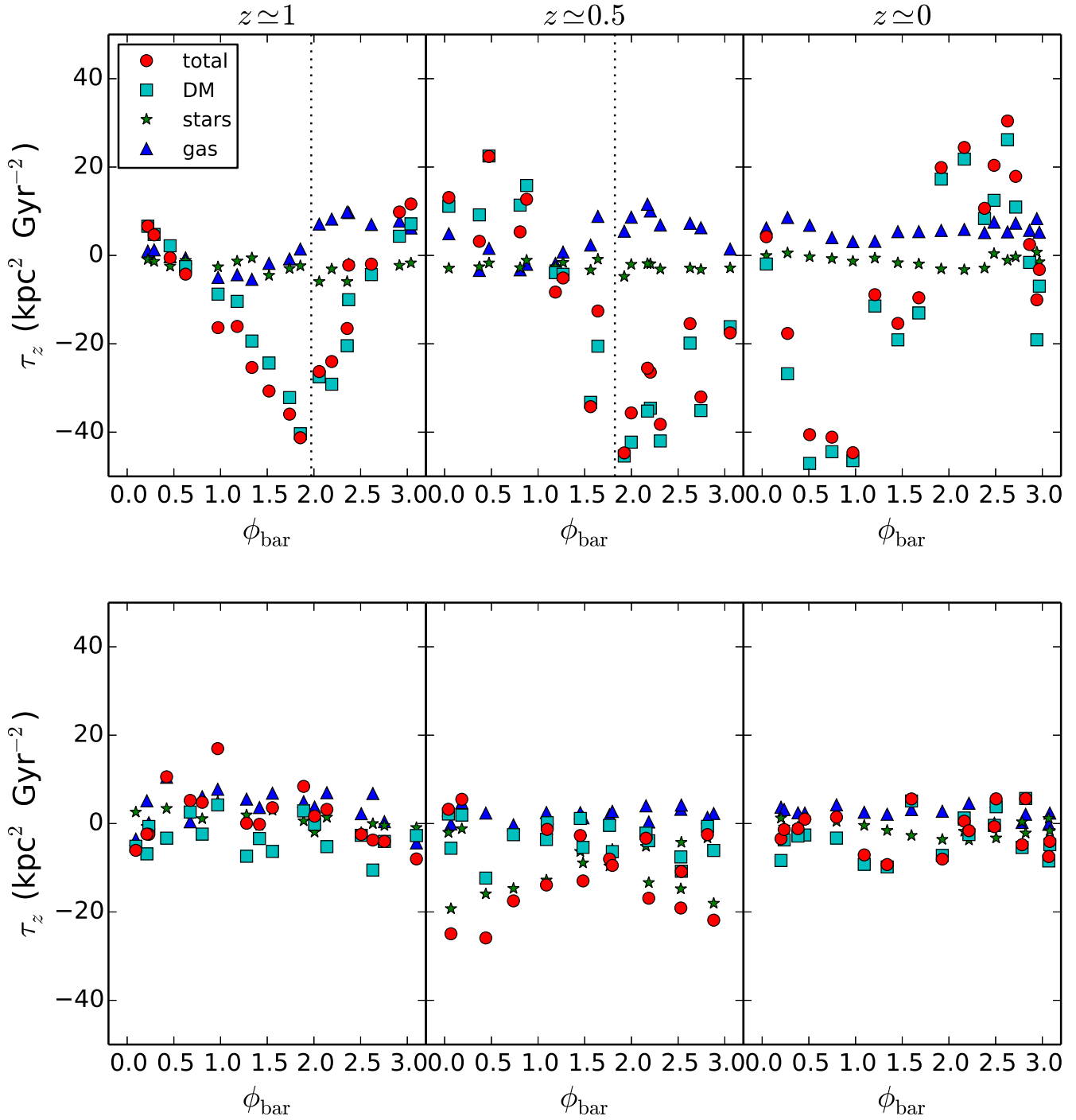


Fig. 7. The z -component of the specific gravitational torque acting on the stars in the bar regions at $z \simeq 1$, 0.5, and 0. The upper and lower panels show Aq-C and Aq-D, respectively. The red circles indicate torque from all the particles within virial radius, r_{vir} . The cyan squares, green stars, and blue diamonds respectively show the contributions of the dark matter, stars, and gas. The vertical dotted lines in the upper left and the upper middle panels indicate the bar angle at which the bar pattern speed is the smallest.

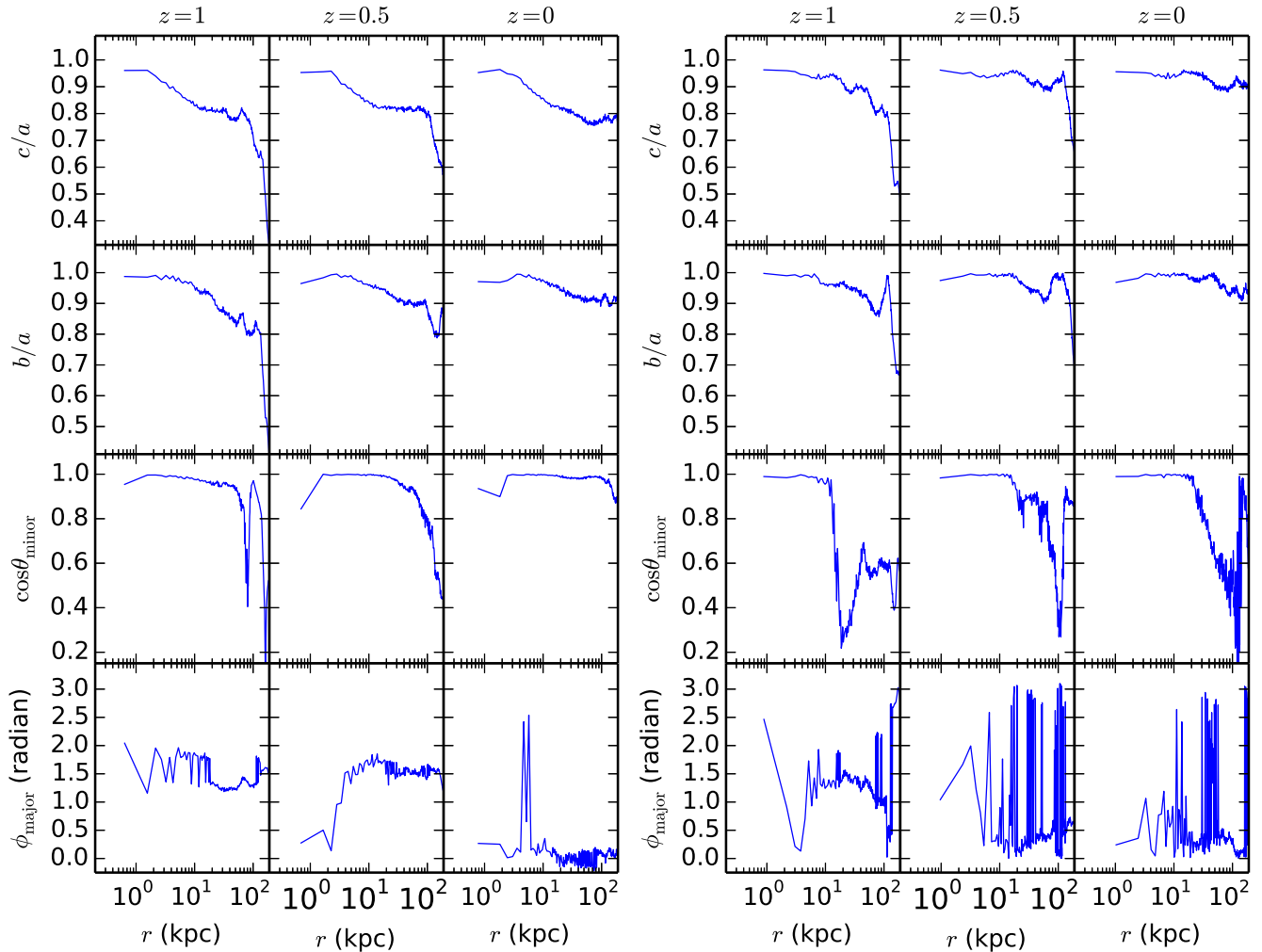


Fig. 8. Radial profiles of the halo triaxiality. The left panels show the halo properties of Aq-C and the right ones show those of Aq-D. From top to bottom, we display the radial profiles of the minor-to-major axial ratio, c/a , the intermediate-to-major axial ratio, b/a , the directional between the disc rotation axis and the halo minor axis, and the azimuthal direction of the halo major axis. From left to right, we show the halos at $z = 1, 0.5,$ and 0 for each galaxy.

action between a bar and its host triaxial halo. They find that A_2^{\max} has a minimum and the halo intermediate-to-major axial ratio, b/a , has a maximum when the bar and halo major axis are aligned. On the other hand, A_2^{\max} has a maximum and the halo b/a has a minimum when the bar and halo major axis are perpendicular. These results imply that the triaxial halo plays a role of an outer bar and the basic building blocks of the bar are loops.

We thus investigate the halo triaxiality in this section. We have removed the subhalos identified by SUBFIND (Springel et al. 2001) in order to consider only the smooth component of the dark halos. The results are however almost identical to the case in which we use the dark matter distribution as it is, except at the outer parts of the dark halos.

In figure 8, we show the radial profiles of the halo triaxiality, where each radial bin contains 20000 dark matter particles. The inner halo has a higher sphericity than the outer halo and the inner halo’s minor axis is well aligned

with the disk rotation axis. The direction of the minor axis of the outer halo is almost independent from that of the inner halo. The baryonic contraction due to gas cooling makes the inner halo more spherical than dark matter only simulations (Kazantzidis et al. 2004; Bailin et al. 2005). The tidal torque between the disk and the inner halo aligns the rotation axis and the halo minor axis (Bailin et al. 2005). We also find that Aq-D’s halo is more spherical than Aq-C’s. This explains the small amplitude of the specific torque from dark matter acting on the bar in Aq-D.

We now explore the time oscillations of the halo triaxiality of Aq-C that shows oscillations in the bar amplitude and pattern speed at high redshift. Athanassoula & Misiriotis (2002) claim that the halo triaxiality should be measured in a density bin instead of a radial bin since the former is noisier than the latter. It is however not the case in our simulations probably because the dark matter density distribution in cosmological halos are not as smooth

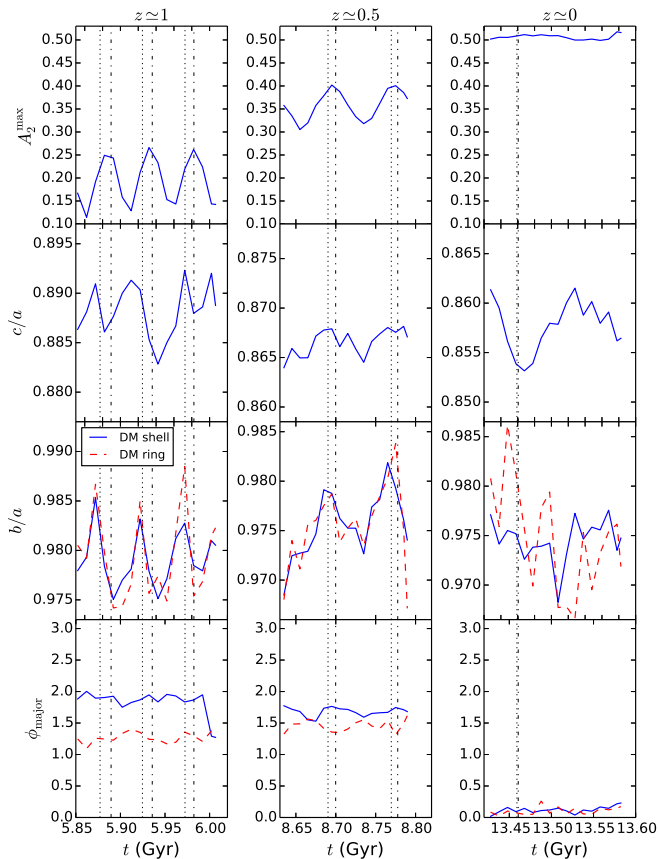


Fig. 9. Time evolutions of the bar amplitude and the halo triaxiality of Aq-C around $z = 1, 0.5$ and 0 (from left to right). From top to bottom, we present the bar amplitude, A_2^{\max} , the minor-to-major halo axial ratio, c/a , the intermediate-to-major halo axial ratio, b/a , and the azimuthal direction of the halo major axis, ϕ_{major} . We also show the axis ratio of the dark matter ring in the disk plane and the azimuthal direction of its major axis by the red dashed lines. The vertical dashed lines indicate the time when the directions of the halo major axis and the bar are aligned and the vertical dotted lines indicate the time when the directions of the major axis of the dark matter ring and bar are aligned.

as that in the idealized simulations even if we remove the subhalos. We hence measure the triaxiality of a spherical shell of radius between r_{bar} and $2r_{\text{bar}}$, where we employ the mean bar length during each simulation as r_{bar} . We first sort the dark matter particles by the distance from the center and identify the ranking of the particles that lie between r_{bar} and $2r_{\text{bar}}$ in the first snapshot. In the rest of the snapshots, we use the dark matter particles that have the same ranking in radius as the particles selected in the first snapshot to measure the orientation and the shape of the halo. Our results are not sensitive to the choice of the radius of the shell as long as that lies between r_{bar} and $3r_{\text{bar}}$. Within r_{bar} , the direction of the halo major axis largely oscillates, but not rotates. In the outer part, ($r \gtrsim 3r_{\text{bar}}$), the direction of the major axis of the halo is independent of that of the inner part (figure 8). Since the minor axis of the halo is not parallel to the rotation axis of the disk as shown in figure 8, the azimuthal direction

of the major axis of the halo can be different from that of the major axis of the dark matter distribution in the disk plane as we will show later. We thus measure the axis ratio of the dark matter ring of $r_{\text{bar}} < r < 2r_{\text{bar}}$ and $|z| < 0.1h^{-1}$ kpc and the direction of its major axis, too.

In figure 9, we show the time evolution of the bar amplitude, the minor-to-major halo axial ratio, and the intermediate-to-major halo axial ratio, together with the axial ratio of the dark matter ring. We also show the azimuthal directions of the major axes of the dark matter shell and ring. The directions of these axes are better aligned at lower redshift simply because the directions of the halo minor axis and the disk rotation axis are better aligned at lower redshift as shown in figure 8.

We find that the axial ratios, b/a , of the shell and ring oscillate with the same frequency as the bar oscillation. The minor-to-major axial ratio, c/a , also shows similar oscillations to b/a . These results agree with the finding by Athanassoula et al. (2013).

The bar amplitude is however largest when the bar and the major axis of the dark matter ring are parallel. This behavior contradicts the result by Athanassoula et al. (2013) and the loop concept that predicts a loop corresponding to an inner bar is less elongated when the inner and outer bars are aligned (Maciejewski & Sparke 2000; Maciejewski & Athanassoula 2007). The simulation results by Heller et al. (2001) and Heller et al. (2007b) are more analogous to ours. They find that the inner bar/ring component is more elongated when it is parallel to the outer bar. On the other hand, the halo is more axisymmetric, i.e. c/a and b/a are large, when the bar and the major axis of the dark matter ring are aligned. This result is consistent with the behaviors of the halo triaxiality found by Athanassoula et al. (2013). Further studies are needed to understand the origin of the disagreement among the simulations.

3.6. Interaction with the $m = 4$ Fourier mode

In this subsection, we investigate the second most significant Fourier mode, the $m = 4$ mode, and explore possible interaction between the $m = 2$ and $m = 4$ Fourier modes. In figure 10, we plot the amplitude and the phase profiles of the $m = 4$ Fourier mode. Since the phase of the $m = 4$ mode, $\phi_4(r)$, is defined between 0 and $\pi/2$, we also plot $\phi_4(r) + \pi/2$ to investigate the alignment between $m = 4$ and 2 modes. Note that as Aq-C’s snapshot at $z \simeq 1$, we chose the one in which the misalignment between the two components is evident.

We find that the relative importance of the $m = 4$ component to the $m = 2$ component is larger in Aq-C than in Aq-D. This result is consistent with those obtained by many simulations. In Athanassoula & Misiriotis (2002), the relative importance of the higher order even moments is higher in a galaxy with a stronger bar. The same trend is seen in cosmological bars (Scannapieco & Athanassoula 2012). In Aq-C, the maxima of $A_4(r)$ occur at almost the same radii as the maxima of $A_2(r)$, i.e. at r_2^{\max} . Usually in idealized simulations, the maxima of the amplitudes of the higher order even moments occur considerably larger radii

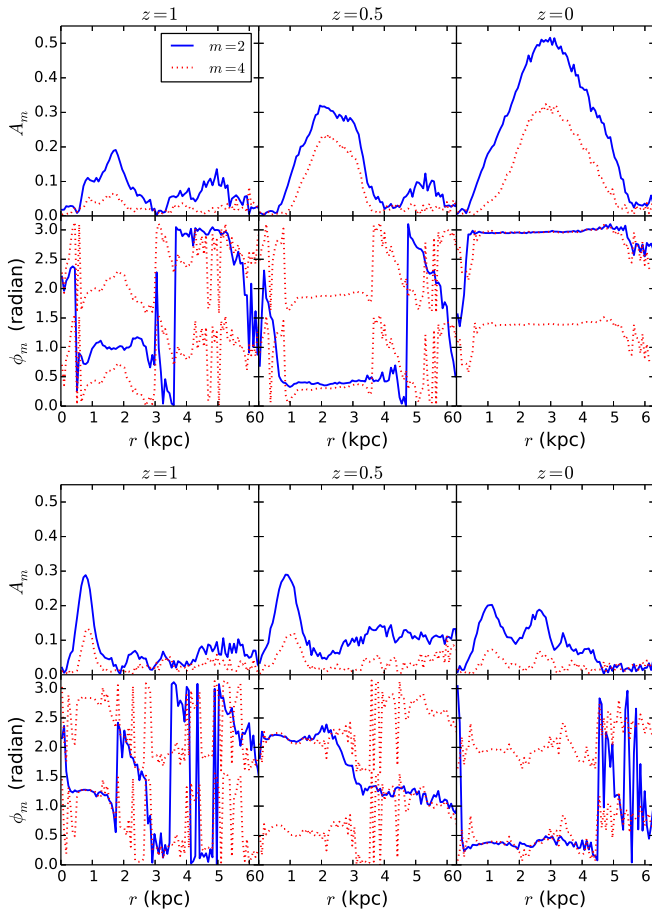


Fig. 10. The amplitude and phase profiles of the $m = 2$ and $m = 4$ modes. The upper and lower six panels show Aq-C and Aq-D, respectively. The blue solid and red dotted lines respectively represent the $m = 2$ and $m = 4$ modes. The amplitude and phase are shown in the upper and lower panels of each group of panels. From left to right, the results at $z = 1$, 0.5, and 0 are presented. For the phase, $\phi_4(r)$, we also plot $\phi_4(r) + \pi/2$ in order to compare it with the $m = 2$ mode.

than r_2^{\max} in galaxies with massive halos (Athanasoula & Misiriotis 2002; Athanasoula 2003). Scannapieco & Athanasoula (2012) obtain the same result as ours for the same Aquarius halo, Aq-C, in spite of their lower resolution and weaker feedback, i.e. a heavier disk, than ours (Scannapieco et al. 2009). This agreement implies that the halo formation history and its shape play an important role in shaping substructure of a galaxy.

In Aq-C, the $m = 2$ component is largely misaligned with the $m = 4$ component at $z = 1$ and is slightly misaligned at $z = 0.5$. At $z = 0$ the two modes are perfectly aligned with each other. On the other hand, the two modes are always aligned in Aq-D. It is interesting that the bar and the $m = 4$ component are misaligned when the bar shows large oscillations in its pattern speed and amplitude.

Next, we explore the relation between the pattern speed and amplitude of the $m = 2$ and $m = 4$ components. To calculate the pattern speed of the $m = 4$ component, we

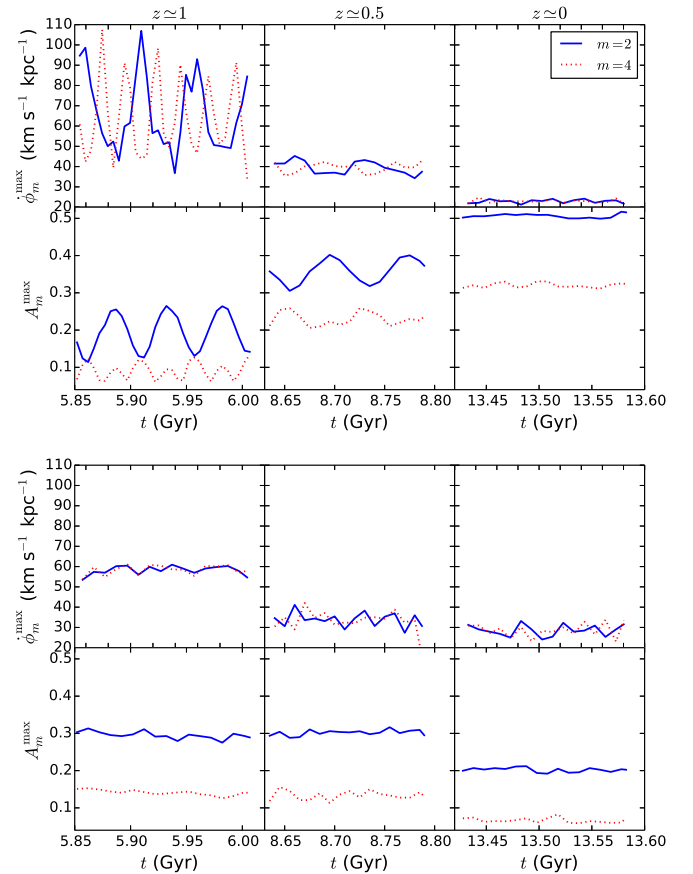


Fig. 11. Same as figure 5 but we now show the pattern speed and amplitude of the $m = 4$ components as well. The $m = 2$ and $m = 4$ components are respectively represented by the blue solid and red dotted lines.

define A_4^{\max} and r_4^{\max} by exactly the same way as we defined A_2^{\max} and r_2^{\max} and then we define the phase of the $m = 4$ component as $\phi_4(r_4^{\max})$.

In figure 11, we show the pattern speed of the $m = 2$ component, $\Omega_{\text{bar}} \equiv \dot{\phi}_{\text{bar}}$, and the $m = 4$ component, $\dot{\phi}_4(r_4^{\max})$. We find that the pattern speed of the $m = 4$ component also shows large and periodic oscillation at $z \simeq 1$ in Aq-C. This oscillation becomes much smaller at $z \simeq 0.5$ at which the misalignment between the two modes is small (see figure 10). Once the phases of the two components are perfectly aligned with each other, the pattern speed of the both components becomes almost constant and of course the two components have the same pattern speed.

The amplitude of the $m = 4$ component also varies with the same frequency as the pattern speed. As for the $m = 2$ component, the amplitude becomes large when the pattern speed is small and vice versa. The frequency of the oscillation of the pattern speed of the $m = 4$ component is clearly higher than that of the $m = 2$ component. We find that the period of the oscillations of the pattern speed and the amplitude of the $m = 4$ component is a quarter of its revolution period.

As we have shown, the $m = 2$ and $m = 4$ components in

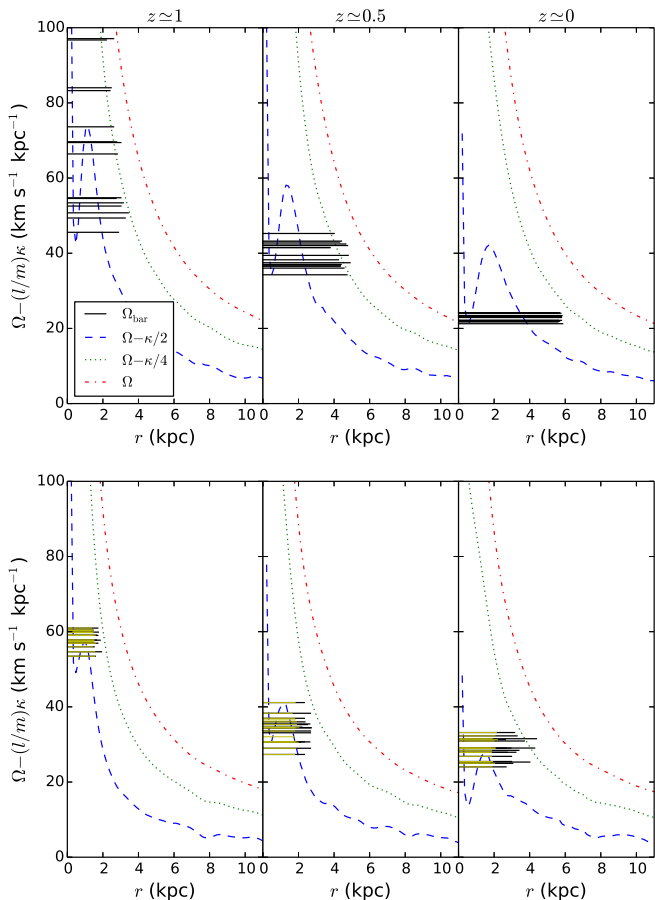


Fig. 12. Behavior of $\Omega - \kappa/2$, $\Omega - \kappa/4$ and Ω at $z = 1, 0.5$, and 0 . The blue dashed, green dotted, and red dot-dashed lines respectively represent $\Omega - \kappa/2$, $\Omega - \kappa/4$, and Ω . The upper and lower panels indicate Aq-C and Aq-D, respectively, and redshifts are $1, 0.5$, and 0 from left to right. We show the bar pattern speed around these redshifts by the horizontal black solid lines, whose lengths correspond to the bar lengths. For Aq-D, we also show the case in which we define the bar lengths by excluding the outer component (horizontal yellow solid lines).

Aq-D are always aligned with each other. In this case, the pattern speed and the amplitude of both $m = 2$ and $m = 4$ components do not show the periodic oscillations, which are seen in Aq-C at $z \simeq 1$ and 0.5 . The high-frequency oscillations are probably caused by the interactions with clumps as we have already discussed for the $m = 2$ mode. Our results suggest that the pattern speed of the bar oscillates if its phase is misaligned with the phase of the $m = 4$ component in the same region.

3.7. Resonances and the bar length

Finally we investigate the resonance structure of the simulated galaxies. In figure 12 we show the behaviors of $\Omega - \kappa/2$, $\Omega - \kappa/4$, and Ω as functions of radius, where Ω is the angular frequency of a circular orbit and κ is the radial angular frequency.

The sharp rise of the $\Omega - \kappa/2$ curves towards the center is due to the gravitational softening. Since the spatial

extent of this region is much smaller than the scale we are interested in, we will ignore the innermost 2:1 resonance due to this sharp rise in the following discussion. Each $\Omega - \kappa/2$ curve has a peak and thus these galaxies have double ILRs if the bar pattern speed is smaller than the peak value (and if we ignore the inner most ILR). The peak values decrease with time since the central density of the galaxies decrease with time due to the stellar evolution and the feedback (see figure 1).

The density structure does not change on the short time-scale during which we measure the pattern speed of the bars around $z = 1, 0.5$, and 0 . We show the bar pattern speed and the bar length measured around these redshifts by the horizontal lines. From the behavior of the bar pattern speed and the amplitude in Aq-C around $z = 1$ and 0.5 , we speculate that the smaller the pattern speed is, the larger the amplitude is if the $\Omega - \kappa/2$ curve is fixed (Kormendy 2013).

On the long time-scale, $\Omega - \kappa/2$ curve is lowered as shown in figure 12. In Aq-C, the bar pattern speed strongly decreases from $z = 1$ to 0 . As a result, the bar amplitude becomes larger with time (figure 4). In Aq-D, the slow down rate of the bar pattern speed is much lower than that in Aq-C. Consequently, the peak value of $\Omega - \kappa/2$ curve decreases as fast as or faster than the bar pattern speed. The bar amplitude in this case does not change much or becomes smaller as shown in figure 4. At $z \simeq 0$, there is no 2:1 resonances in many cases if we ignore the inner most resonance. As a result, the bar amplitude at $z = 0$ is smaller than that at $z = 0.5$. We will discuss the sharp decline in the amplitude of Aq-D's bar at $t \sim 9.8$ Gyr shown in figure 4 in the next section.

The bar lengths are around the 4:1 resonances in both galaxies at all redshifts. Even if we define the length of Aq-D's bar by excluding the outer component, the bar looks terminated at this resonance except at $z \simeq 0$. Patsis et al. (1997) study the orbital structure in the potential model of NGC 4314 and predict that the longest stable periodic orbits are found at the 4:1 resonance. Our cosmological simulations confirm their prediction.

4. Discussion and conclusions

We have investigated the cosmological evolution of bars by utilizing the two Milky Way-mass galaxies formed in the fully self-consistent simulations of the galaxy formation by Okamoto (2013). The evolution qualitatively agrees with what is expected from idealized simulations, that is, the bar in the galaxy having more centrally concentrated mass distribution exhibit stronger evolution than the other (Combes & Elmegreen 1993; Athanassoula 2003). This picture is in good agreement with observations (e.g. Cheung et al. 2013). The bar in Aq-C receives the large negative torque from the dark matter and is significantly slowed down $z = 1$ to 0 . As the bar pattern speed decreases, the bar becomes stronger and longer. On the other hand, the torque acting on Aq-D's bar is much weaker by lacking materials that absorb the angular momentum of the bar.

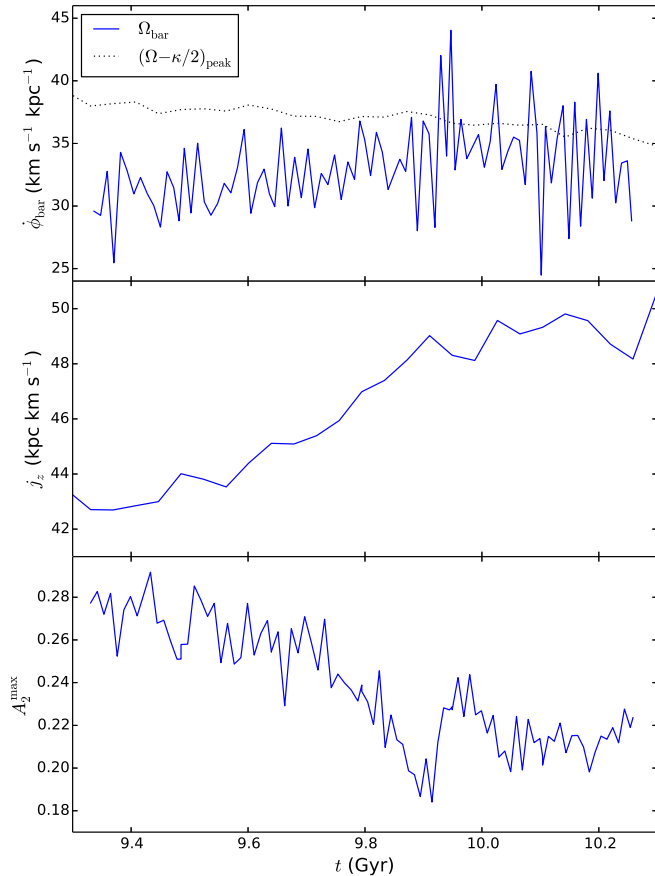


Fig. 13. Evolution of the bar pattern speed and amplitude of Aq-D around $t \simeq 9.8 \text{ Gyr}$. In the top panel, we show the evolution of the bar pattern speed and the peak value of the $\Omega - \kappa/2$ curve by the blue solid and black dotted lines respectively. In the middle panel we also plot the specific angular momentum of the stars in the bar region ($r < 1.68 \text{ kpc}$ and $|z| < 1 \text{ h}^{-1} \text{ kpc}$). In the bottom panel, we show the bar amplitude $A_2^{\text{max}}(t)$.

The pattern speed of Aq-C’s bar violently oscillates at $z \simeq 1$. The oscillation becomes smaller at $z \simeq 0.5$ and disappears at $z \simeq 0$. The period of the oscillation as a function of the bar angle is π , indicating the interaction with the halo’s quadrupole moment. The amplitude of the bar also shows the oscillations with the same frequency as those of the pattern speed. When the bar rotates slower, it becomes stronger and vice versa. This short-term behavior is consistent with the long-term behavior in Aq-C, i.e. the slower the bar rotation is, the larger its amplitude is. These oscillations correlate with the oscillations in the halo triaxiality as pointed out by Athanassoula et al. (2013). When the bar and the halo major axis are parallel, the halo is more spherical and the bar is strongest. The former result agrees with the simulations by Athanassoula et al. (2013), but the latter is opposite to them. The origin of the disagreement is unclear.

The evolution of the bar in Aq-D seems to contradict this scenario. While the pattern speed of the bar decreases

with time, its amplitude does not increase from $z = 1$ to 0.5 and even decreases from $z = 0.5$ to 0 . We speculate that this is because the $\Omega - \kappa/2$ curve is lowered with time (figure 12) due to the decreasing central density with time (figure 1), which is most likely caused by the mass loss and feedback from the stellar populations. The inclusion of the mass loss through the entire life of stellar populations and strong feedback is one of the biggest differences between our cosmological simulations and idealized simulations of isolated galaxies. The instantaneous recycling approximation is often used in idealized simulations and old stars do not lose their mass even when gas cooling, star formation, and feedback are included in idealized simulations (e.g. Athanassoula et al. 2013). Thanks to the efficient angular momentum transfer from the bar to the dark matter in Aq-C, the bar pattern speed drops faster than the $\Omega - \kappa/2$ curve, and thus the bar becomes stronger. On the other hand, the slowdown rate of Aq-D’s bar is as low as the decreasing rate of the peak value of the $\Omega - \kappa/2$ curve.

In Aq-D, the amplitude of the bar sharply drops at $t \sim 9.8 \text{ Gyr}$. To see why the bar is weakened, we measure the bar pattern speed and the peak value of the $\Omega - \kappa/2$ curve, $(\Omega - \kappa/2)_{\text{peak}}$, around this epoch. In figure 13, we show the evolution of the bar pattern speed by restarting the simulations from several snapshots and compare it with the evolution of $(\Omega - \kappa/2)_{\text{peak}}$.

We find that the bar pattern speed is in fact an increasing function of time on average until $t \simeq 9.9 \text{ Gyr}$, while $(\Omega - \kappa/2)_{\text{peak}}$ slowly decreases with time. As the bar pattern speed approaches $(\Omega - \kappa/2)_{\text{peak}}$, the bar amplitude decreases. We also show the evolution of the specific angular momentum of the stars in the bar region ($r < 1.68 \text{ kpc}$). The specific angular momentum in the bar region sharply increases with time until $t \simeq 9.9 \text{ Gyr}$. The angular momentum is most presumably brought by the clumps. Okamoto (2013) has shown that a non-negligible amount of mass is added to Aq-D’s bulge by the clumps during this epoch. The high frequency oscillations in the bar pattern speed are likely to be caused by the interactions with the clumps. At $t \gtrsim 9.9 \text{ Gyr}$, the bar pattern speed often exceeds $(\Omega - \kappa/2)_{\text{peak}}$. These results support the idea that the bar amplitude is determined by the relation between the pattern speed and the $\Omega - \kappa/2$ curve.

Interestingly, the oscillations in the bar pattern speed and amplitude in Aq-D’s bar are observed only when the $m = 2$ component is misaligned with the $m = 4$ component. The oscillations become smaller as the two components get aligned with each other. The $m = 4$ components have the comparable spatial size to the $m = 2$ components in both galaxies.

The bar lengths seem to be determined by the 4:1 resonances. Our cosmological simulations thus confirm the prediction by Patsis et al. (1997). Our results are also consistent with the observation of NGC 253, which has a bar whose length coincides with 4:1 resonance (Sorai et al. 2000).

In summary, using high-resolution cosmological simulations of disk galaxy formation, we show that the bar evolution in the cosmological simulations is qualitatively

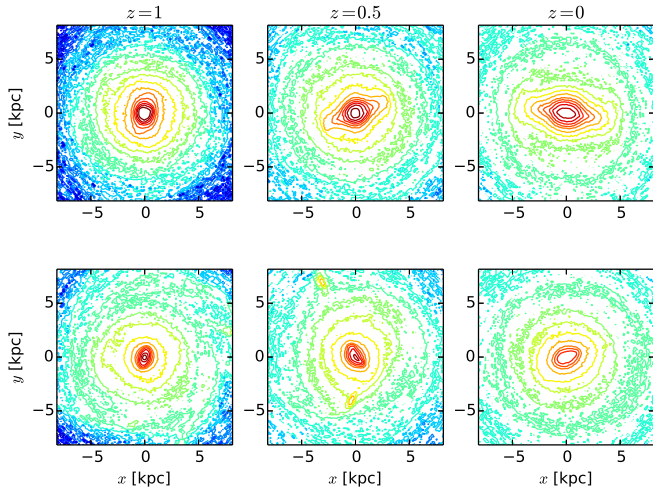


Fig. 14. The same as figure 3, but shown the original surface stellar density maps where the clumps are not removed).

consistent with that obtained by idealized simulations of isolated disk galaxies and observations. We find that the strong feedback and continuous mass loss from stellar populations significantly lowers the central density with time and hence changes the resonance structure. We also find that the clumps formed in the disk can spin up the bar and can weaken its strength. Our sample is too small to understand why the oscillations in bar amplitude correlate with those in halo triaxiality differently from the idealized simulations by Athanassoula et al. (2013) and thus we leave it for future studies.

We are grateful to the anonymous referee for the careful reading of the manuscript and the thoughtful comments. We would like to thank Masafumi Noguchi and Junich Baba for helpful discussion. We also thank John Kormendy, Françoise Combes, and Shunsuke Hozumi for useful comments on the manuscript. Numerical simulations were carried out with Cray XC30 in CfCA at NAOJ and T2K-Tsukuba in Center for Computational Sciences at University of Tsukuba. TO acknowledges the financial support of Japan Society for the Promotion of Science (JSPS) Grant-in-Aid for Young Scientists (B: 24740112).

Appendix 1. Clump removal

In order for the $m=2$ component not to include contributions from clumps, we have removed the clumps from the density field before we calculate the Fourier series. In figure 14, we present the original surface stellar density maps. There are clearly two clumps in Aq-D at $z=0.5$, which are not seen in figure 3 where we have eliminated the contribution of the clumps.

To remove the clumps, we start from the cell that has the highest surface stellar density and then examine its neighboring cells. If the surface density of a neighboring cell is equal to or lower than that of the current cell, we add it to the *smooth* component. By recursively examin-

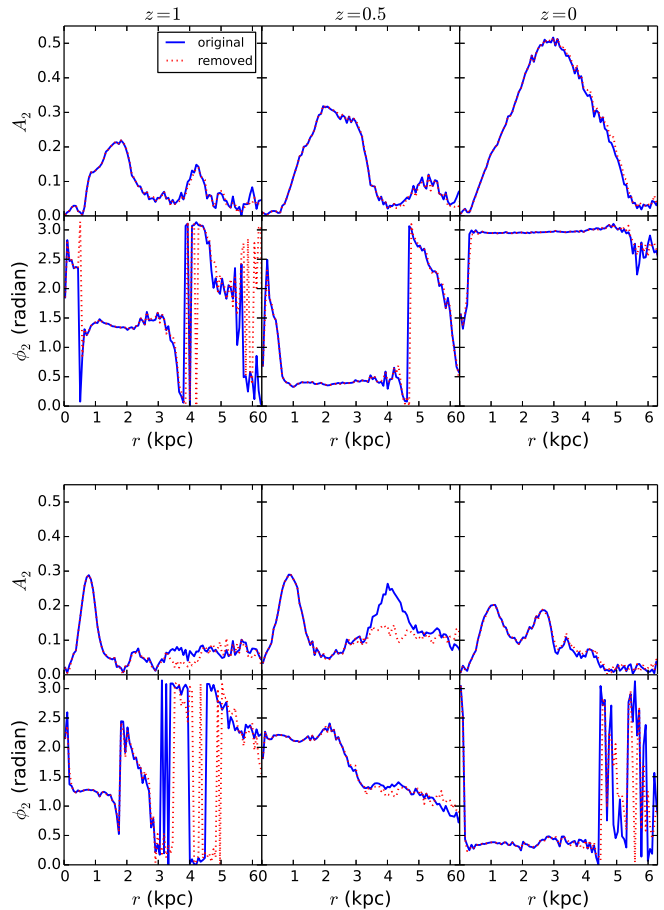


Fig. 15. The same as figure 2 but here we compare the amplitude and phase profiles from the original surface stellar density fields (blue solid lines) with those from the density fields in which the clumps have been removed (red dotted lines).

ing the neighboring cells of the smooth component, local density peaks are isolated as non-smooth components.

We then replace the surface density of the cell at (r, ϕ) , classified as the non-smooth components with that of the cell at $(r, \phi + \pi)$. This method has an advantage that it can be applied even when a clump is at radius comparable to or smaller than the bar length. We have applied this procedure to all the simulation snapshots used in this paper.

In figure 15, we compare the amplitude and phase profiles of the $m=2$ mode obtained from the original surface stellar density fields with those obtained from the density field in which the clumps have been removed. We find that the profiles are almost indistinguishable when there is no irregular structure like clumps. Hence the procedure described above does not affect our results when the clumps do not exist.

At $z=0.5$ in Aq-D, the clumps shown in figure 14 contribute to the $m=2$ mode. Removing the clumps lowers the second peak in the amplitude profile. The phase profile is however hardly affected by the clump removal, since the arm-like features induced by the clumps remain

present in the surface stellar density (see figure 3).

We have confirmed that the removal of the clumps does not affect our estimation of the bar length, amplitude, and phase for all the snapshots used in the paper. Nevertheless, we apply the clump removal procedure all the analyses present in this paper, unless otherwise stated.

Appendix 2. Bar length

Athanassoula & Misiriotis (2002) presented a number of ways to measure bar length. Scannapieco & Athanassoula (2012) tested three of them, which are applicable to cosmological simulations. We here use these three methods and see the uncertainties in measuring the bar length.

The first method is the one we employ in the main text, which utilizes the radial phase profile of the $m = 2$ Fourier component. This method gives the bar length 5.58 kpc for Aq-C and 4.42 kpc for Aq-D at $z = 0$.

In the second method, we utilize the amplitude of the $m = 2$ Fourier component. We estimate the bar length from the radius where the $m = 2$ amplitude drops to a small fraction of A_2^{\max} . We here define the bar length as the radius where $A_2(r)$ drops to $0.25A_2^{\max}$ as done in Scannapieco & Athanassoula (2012). The bar lengths given by this method are 5.17 kpc and 4.42 kpc for Aq-C and Aq-D, respectively, at $z = 0$.

The third method utilizes the surface stellar density profiles shown in figure 16. Within the bar length, the surface density along the bar major axis must be higher than that along the minor axis at given radius. For Aq-C, we can see the clear signature of the bar in the surface density profiles. On the other hand, the signature is much weaker for Aq-D. This is consistent with the small amplitude of the $m = 2$ Fourier mode in Aq-D. We define the bar length as the radius where the relative difference between the surface densities along the major and minor axes drops to 10 % of the maximum. This method yields the bar length of 5.65 kpc for Aq-C and 4.49 kpc for Aq-D as indicated in figure 16 by the vertical lines.

The bar lengths obtained by the three different methods agree reasonably well between them both for Aq-C and Aq-D. We thus only show the bar length obtained by the first method in the main text.

Appendix 3. The outer component of Aq-D's bar

As we discussed in the main text, Aq-D's bar at $z = 0$ has two peaks in the amplitude of the $m = 2$ component within the bar length. This is quite unusual and thus we here present the evolution and properties of the outer component.

In figure 17, we show the evolution of the amplitude and the phase of the outer $m = 2$ component of Aq-D around $z = 0$. We find that the amplitude largely varies with time, while the amplitude of the inner peak does not change much (see figure 5).

We also show the phase of the outer $m = 2$ component. Clearly, the outer component is almost always aligned with the inner component, though the slight misalignment

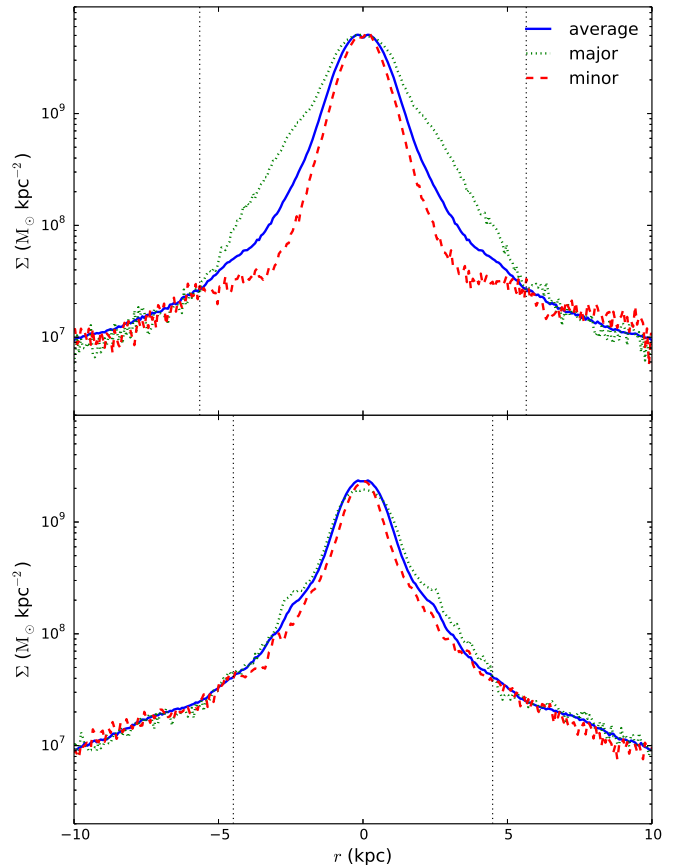


Fig. 16. Surface stellar density profiles at $z = 0$, when galaxies seen face-on. The upper and lower panels respectively show Aq-C and Aq-D. The azimuthally averaged profile is shown by the blue solid line, and the profiles along the bar major axis and minor axis are shown by the green dotted and red dashed lines, respectively. The vertical dotted lines indicate the bar lengths defined by the surface stellar density profiles.

at $t < 13.53$ Gyr is too large to include the outer component in the bar. Therefore, the outer component might be a part of the bar whose amplitude is enhanced and phase is shifted by the interactions with other components.

We show the face-on surface stellar density maps of Aq-D at $t \simeq 13.54$ Gyr when the amplitude of the outer $m = 2$ component is the largest. To see what is happening more closely, we draw contours that indicate the densities at radii corresponding to the minimum and outer peak of $A_2(r)$. The contours for the original density distribution clearly show the existence of substructure at the radius corresponding to the outer peak of $A_2(r)$. We always find such substructure when the amplitude of the outer component takes the maxima. The high frequency oscillation seen in the time evolution of the amplitude of the outer peak (see figure 17) suggests that the outer peak is induced by objects that are orbiting in the disk with different angular velocity from the bar. We suspect that these rotating objects are debris of clumps from the surface density contours.

After we have removed the clumps, we do not see such

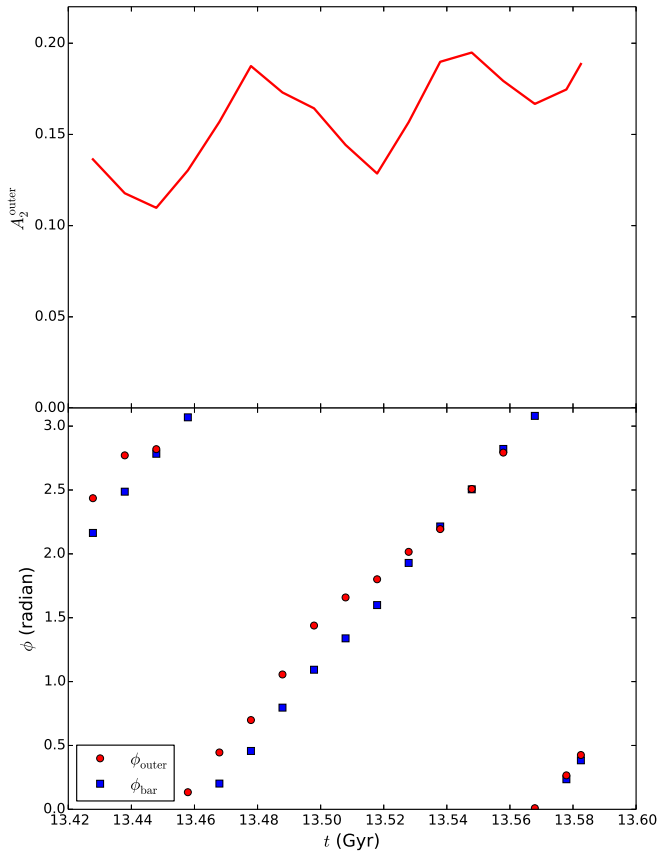


Fig. 17. *Upper panel:* the amplitude of the $m=2$ component in Aq-D at the radius corresponding to the outer peak in the amplitude profile. *Lower panel:* The phase of the outer peak in the amplitude profile of the $m=2$ component of Aq-D (red filled points). The phase of the bar, i.e. the phase at the radius corresponding to the inner peak in the amplitude profile, is indicated by the blue filled squares.

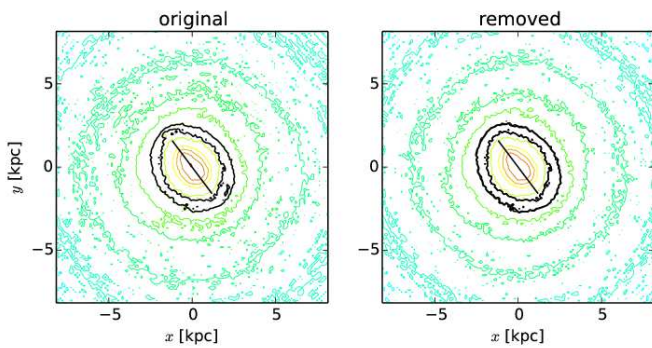


Fig. 18. Contour maps of the face-on stellar surface density of Aq-D when the amplitude of the outer $m=2$ component is maximum ($t \simeq 13.54$ Gyr). The left and right panels respectively show the original density field and the one in which the clumps have been removed. The inner thick black solid contour corresponds to the densities at the radius where $A_2(r)$ takes the minimum value between two peaks. The outer thick black contour indicates the density at the radius of the outer peak. Here the bar length (the black straight line) is terminated at the radius where $A_2(r)$ takes the minimum value between two peaks.

substructure in the density distribution (right panel of figure 3). The amplitude of the $m=2$ component however has a peak at the same radius even if we have removed the clumps because our procedure to remove the clumps do not erase the features induced by interactions with the clumps. When the amplitude of the outer component is smallest, the amplitude profile of the $m=2$ component is similar to that of a weak bar whose length is beyond the radius of the outer peak, although the amplitude profile is very noisy. We therefore do not exclude the outer $m=2$ component from the bar as long as its phase is aligned with ϕ_{bar} , i.e. the phase of the inner peak. We stress that the bar angle, ϕ_{bar} , and the bar amplitude, A_2^{max} , are not affected by the inclusion (or exclusion) of the outer component because we always employ the radius of the inner peak as r_2^{max} .

References

- Athanassoula, E. 2003, MNRAS, 341, 1179
— 2005, MNRAS, 358, 1477
— 2008, MNRAS, 390, L69
— 2013, Bars and secular evolution in disk galaxies: Theoretical input, ed. J. Falc3n-Barroso & J. H. Knapen, 305
- Athanassoula, E., Machado, R. E. G., & Rodionov, S. A. 2013, MNRAS, 429, 1949
- Athanassoula, E., & Misiriotis, A. 2002, MNRAS, 330, 35
- Bailin, J., Kawata, D., Gibson, B. K., et al. 2005, ApJL, 627, L17
- Barazza, F. D., Jogee, S., & Marinova, I. 2008, ApJ, 675, 1194
- Behroozi, P. S., Wechsler, R. H., & Conroy, C. 2013, ApJ, 770, 57
- Berentzen, I., Athanassoula, E., Heller, C. H., & Fricke, K. J. 2004, MNRAS, 347, 220
- Buta, R., Laurikainen, E., Salo, H., Block, D. L., & Knapen, J. H. 2006, AJ, 132, 1859
- Buta, R. J., Knapen, J. H., Elmegreen, B. G., et al. 2009, AJ, 137, 4487
- Cheung, E., Athanassoula, E., Masters, K. L., et al. 2013, ApJ, 779, 162
- Combes, F., Debbasch, F., Friedli, D., & Pfenniger, D. 1990, A&A, 233, 82
- Combes, F., & Elmegreen, B. G. 1993, A&A, 271, 391
- Combes, F., & Sanders, R. H. 1981, A&A, 96, 164
- Curir, A., Mazzei, P., & Murante, G. 2006, A&A, 447, 453
- Debattista, V. P., Carollo, C. M., Mayer, L., & Moore, B. 2004, ApJL, 604, L93
- Debattista, V. P., & Sellwood, J. A. 2000, ApJ, 543, 704
- Dubinski, J., Berentzen, I., & Shlosman, I. 2009, ApJ, 697, 293
- Duffy, A. R., Schaye, J., Kay, S. T., et al. 2010, MNRAS, 405, 2161
- Efstathiou, G., Lake, G., & Negroponte, J. 1982, MNRAS, 199, 1069
- Eke, V. R., Cole, S., & Frenk, C. S. 1996, MNRAS, 282, 263
- Elmegreen, B. G., Elmegreen, D. M., Knapen, J. H., et al. 2007, ApJL, 670, L97
- Eskridge, P. B., Frogel, J. A., Pogge, R. W., et al. 2000, AJ, 119, 536
- Frenk, C. S., White, S. D. M., Davis, M., & Efstathiou, G. 1988, ApJ, 327, 507
- Governato, F., Zolotov, A., Pontzen, A., et al. 2012, MNRAS, 422, 1231

- Guedes, J., Callegari, S., Madau, P., & Mayer, L. 2011, *ApJ*, 742, 76
- Guo, Q., White, S., Li, C., & Boylan-Kolchin, M. 2010, *MNRAS*, 404, 1111
- Heller, C., Shlosman, I., & Englmaier, P. 2001, *ApJ*, 553, 661
- Heller, C. H., Shlosman, I., & Athanassoula, E. 2007a, *ApJL*, 657, L65
- . 2007b, *ApJ*, 671, 226
- Jing, Y. P., & Suto, Y. 2002, *ApJ*, 574, 538
- Kazantzidis, S., Kravtsov, A. V., Zentner, A. R., et al. 2004, *ApJL*, 611, L73
- Klypin, A., Kravtsov, A. V., Valenzuela, O., & Prada, F. 1999, *ApJ*, 522, 82
- Kormendy, J. 1979, *ApJ*, 227, 714
- . 2013, *Secular Evolution in Disk Galaxies*, ed. J. Falcón-Barroso & J. H. Knapen, 1
- Kormendy, J., & Kennicutt, Jr., R. C. 2004, *ARA&A*, 42, 603
- Kraljic, K., Bournaud, F., & Martig, M. 2012, *ApJ*, 757, 60
- Lynden-Bell, D., & Kalnajs, A. J. 1972, *MNRAS*, 157, 1
- Maciejewski, W., & Athanassoula, E. 2007, *MNRAS*, 380, 999
- Maciejewski, W., & Sparke, L. S. 2000, *MNRAS*, 313, 745
- Marinacci, F., Pakmor, R., & Springel, V. 2014, *MNRAS*, 437, 1750
- Martinez-Valpuesta, I., Shlosman, I., & Heller, C. 2006, *ApJ*, 637, 214
- Miwa, T., & Noguchi, M. 1998, *ApJ*, 499, 149
- Moore, B., Ghigna, S., Governato, F., et al. 1999, *ApJL*, 524, L19
- Moster, B. P., Naab, T., & White, S. D. M. 2013, *MNRAS*, 428, 3121
- Okamoto, T. 2013, *MNRAS*, 428, 718
- Okamoto, T., Eke, V. R., Frenk, C. S., & Jenkins, A. 2005, *MNRAS*, 363, 1299
- Okamoto, T., Frenk, C. S., Jenkins, A., & Theuns, T. 2010, *MNRAS*, 406, 208
- Okamoto, T., Gao, L., & Theuns, T. 2008, *MNRAS*, 390, 920
- Okamoto, T., Shimizu, I., & Yoshida, N. 2014, *PASJ*, 66, 70
- Patsis, P. A., Athanassoula, E., & Quillen, A. C. 1997, *ApJ*, 483, 731
- Pfenniger, D., & Norman, C. 1990, *ApJ*, 363, 391
- Romano-Díaz, E., Shlosman, I., Heller, C., & Hoffman, Y. 2008, *ApJL*, 687, L13
- Salucci, P., Lapi, A., Tonini, C., et al. 2007, *MNRAS*, 378, 41
- Scannapieco, C., & Athanassoula, E. 2012, *MNRAS*, 425, L10
- Scannapieco, C., White, S. D. M., Springel, V., & Tissera, P. B. 2009, *MNRAS*, 396, 696
- Scannapieco, C., Wadepuhl, M., Parry, O. H., et al. 2012, *MNRAS*, 423, 1726
- Sheth, K., Elmegreen, D. M., Elmegreen, B. G., et al. 2008, *ApJ*, 675, 1141
- Sorai, K., Nakai, N., Kuno, N., Nishiyama, K., & Hasegawa, T. 2000, *PASJ*, 52, 785
- Springel, V., White, S. D. M., Tormen, G., & Kauffmann, G. 2001, *MNRAS*, 328, 726
- Springel, V., Wang, J., Vogelsberger, M., et al. 2008, *MNRAS*, 391, 1685
- Stinson, G. S., Brook, C., Macciò, A. V., et al. 2013, *MNRAS*, 428, 129
- Tremaine, S., & Weinberg, M. D. 1984, *MNRAS*, 209, 729
- Weinberg, M. D. 1985, *MNRAS*, 213, 451